On-chip quantum communication devices

Alessandro Trenti, Martin Achleitner, Florian Prawits, Bernhard Schrenk, *Member, IEEE*, Hauke Conradi, Moritz Kleinert, Alfonso Incoronato, Francesco Zanetto, Franco Zappa, Ilaria Di Luch, Ozan Çirkinoglu, Xaveer Leijtens, *Senior member, IEEE*, Antonio Bonardi, Cedric Bruynsteen, Xin Yin, Christian Kießler, Harald Herrmann, Christine Silberhorn, Mathieu Bozzio, Philip Walther, Hannah C. Thiel, Gregor Weihs and Hannes Hübel

(invited paper)

***Abstract*—We present here results of the Quantum Technology Flagship project UNIQORN in the area of integrated photonics for quantum communication applications. Three distinct integration platforms, namely indium phosphide based monolithic integration, polymer-based hybrid integration and the CMOS-compatible silicon platform, have been employed to manufacture components and sub-systems on chip for quantum communication devices. The choice of different platforms was made to exploit the best characteristics of each platform for the intended quantum communication device. The indium phosphide platform was employed to manufacture a transmitter chip for quantum key distribution featuring laser, modulators, and attenuators. The transmitter chip was evaluated in a QKD experiment achieving a secure rate of 1 kbit/s. The polymer platform was investigated for engineering non-classical light sources. Entangled and heralded single-photon sources, based on non-linear optics, were assembled on the polymer in a hybrid fashion together with waveguides and other passive micro-optical elements. A quantum random number generator, featuring a 70% randomness extraction efficiency, was also fabricated using the polymer integration technique. An array of 32 individual single-photon avalanche diodes, operating at room temperature and featuring an onboard coincidence logic, was coupled to the chip to demonstrate direct detection of photons on the polymer. Finally, a transimpedance amplifier based on gallium arsenide high electron mobility transistors was produced with an exceptional large electrical noise clearance of 28 dB at 100 MHz.**

***Index Terms*— Photonic integrated circuits, quantum communication, quantum cryptography, quantum key distribution, quantum entanglement, qubit, random number generator.**

I. Introduction

The second quantum revolution will lead to new Information and Communications Technology (ICT) applications drastically outperforming their current counterparts based on "classical bits". By harnessing the power of quantum physics, the new unit of information, the so-called quantum bit or qubit, can provide additional powers to information processing in the form of superposition, entanglement, but also impose new restrictions such as the non-cloning theorem [1]. These characteristics allow for example quantum computers to exhibit exponential speedups, quantum sensors with highly increased sensitivity or quantum communication protocols that are secure against any kind of attack [2]. In particular for quantum communications applications, where photons are the optimal choice for a physical qubit implementation, the use of photonic integrated circuits (PICs) to reduce the size, weight and power consumption in combination with increased stability is very appealing. Not surprisingly, work on quantum photonic integrated circuits (QPICs), has been greatly expanded over the last decade [3].

The paper here provides an overview on the main achievements of the Quantum Technology flagship project UNIQORN [4] that set out to greatly expand our horizon on the usage of photonic integrated circuits for various quantum communication sub-systems and devices. To span the requirements of different quantum communication devices, different photonic integration technologies were employed;

Manuscript received June 3, 2022. This work has been funded by the European Union's Horizon 2020 research and innovation programme through the Quantum-Flagship project UNIQORN (no. 820474) *(Corresponding author: Alessandro Trenti)*.

Alessandro Trenti, Martin Achleitner, Florian Prawits, Bernhard Schrenk and Hannes Hübel are with the Austrian Institute of Technology, Center for Digital Safety&Security, Giefinggasse 4 1210 Vienna Austria (e-mail: alessandro.trenti@ait.ac.at, martin.achleitner@ait.ac.at; florian.prawits@ait.ac.at; bernhard.schrenk@ait. ac.at hannes.huebel@ait.ac.at). e-mail:).

Hauke Conradi and Moritz Kleinert are with the Fraunhofer Heinrich Hertz Institute, 10587 Berlin, Germany (e-mail: hauke.conradi@hhi.fraunhofer.de; moritz.kleinert@hhi.fraunhofer.de).

Alfonso Incoronato, Francesco Zanetto and Franco Zappa are with Politecnico di Milano, Dipartimento di Elettronica, Informazione e Bioingegneria, Piazza Leonardo DaVinci 32, Milano 20133, Italy (e-mail: alfonso.incoronato@polimi.it; francesco.zanetto@polimi.it; franco.zappa@polimi.it).

Ilaria di Luch is with Photonpath, Via Giovanni Durando 39, Milano 20158, Italy (e-mail: ilaria.diluch@photon-path.com).

Ozan Çirkinoglu and Xaveer Leijtens are with the Eindhoven Hendrik Casimir Institute, Eindhoven University of Technology, 5600 MB Eindhoven, Netherlands (e-mail: h.o.cirkinoglu@tue.nl; x.j.m.leijtens@tue.nl).

Antonio Bonardi is with Smart Photonics, High Tech Campus 29, 5656 AE Eindhoven, Netherlands (e-mail: Antonio.bonardi@smartphotonics.nl)

Cedric Bruynsteen and Xin Yin Yin are with IDLab, imec - Ghent University, Technologiepark-Zwijnaarde 126, 9052 Ghent, Belgium (e-mail: cedric.brynsteen@ugent.be; xin.yin@ugent.be).

Christian Kießler, Harald Herrmann and Christine Silberhorn are with the University of Paderborn, Department of Physics and CeOPP, Warburger Strasse 100, 33098 Paderborn, Germany (e-mail: kiessler@mail.uni-paderborn.de; harald.herrmann@uni-paderborn.de; christine.silberhorn@upb.de).

Mathieu Bozzio and Philip Wlather are with the University of Vienna, Department of Physics, Boltzmanngasse 5 1090 Vienna, Austria (e-mail: mathieu.bozzio@univie.ac.at; philip.walther@univie.ac.at).

Hannah C. Thiel and Gregor Weihs are with the University of Innsbruck, Institut fuer Experimentalphysik Laborgebaeude Nord Technikerstrasse 25d 6020 Innsbruck Austria (e-mail: Hannah.Thiel@uibk.ac.at; Gregor.Weihs@uibk.ac.at).

namely InP-, polymer-, silicon-, and GaAs-based photonic platforms.

The paper is divided into the following sections which reflect the use of photonic integrated circuits in different quantum communication applications: Section II describes a quantum random number generator based on the PolyBoard integration platform together with a hybrid assembly procedure to integrate a single photon avalanche diode (SPAD) array onto the PolyBoard chip. In section III, an optical quantum key distribution (QKD) transmitter generating phase encoded signals on a monolithic InP chip is presented. The chip was evaluated in a full QKD key exchange based on the coherent one-way (COW) protocol. Section IV details the development of an ultra-low noise transimpedance amplifier (TIA). Such a component is vital for the performance of continuous-variable (CV) QKD receivers. In section V, the production of non-classical light sources (entangled and heralded single-photon sources) on chip is described. The QPICs for these sub-systems are based on the polymer platform in combination with non-linear optical elements. Finally, in section VI we draw a conclusion on the applicability of the various integration platforms for quantum communication component manufacturing.

II. POLYMER-BASED INTEGRATED QRNG

The quantum random number generator (QRNG) chip is designed in a polymer photonic integrated circuit, called the PolyBoard [5]. The PolyBoard platform was chosen for its compatibility with Si-based SPADs as in this way the maturity and electronics co-integration offered by CMOS processes can be used. SOI and III-V waveguides cannot be used due to the absorption at the bandgap of the semiconductor, leaving hybrid integration with passive waveguiding platforms such as Si3N4 and polymers with broad spectral transparency as viable option for the realization of these circuits. A polymer-based implementation was chosen for the efficient thermal tunability due to the low thermal conductivity of the material.

The QRNG chip comprises embedded polymer waveguides with a width of 2.9 µm x 2.9 µm and a refractive index difference of Δn=0.011. The waveguide is designed to be single mode at wavelengths around 785 nm. Core and cladding polymer layers are deposited by spin coating of liquid polymer resin, and UV curing and hard baking of the layers. Fabrication of the waveguides and electrode layers is done with photolithographic masks and reactive ion etching. Two designs were fabricated, a 1:4 chip with four outputs and, for higher bitrates, a 1:16 chip. The first version comprises a 1x4 multimode interference coupler (MMI), the 1:16 design cascades two stages of 1x4 MMI to achieve the 1x16 splitting. Fig. 1 depicts the layout of the 1:16 chip. Two additional thermo-optic switches (TOSs) enable the attenuation of the incoming signal. Additional air trenches and metallic layers shield the waveguide outputs from on-chip stray light.

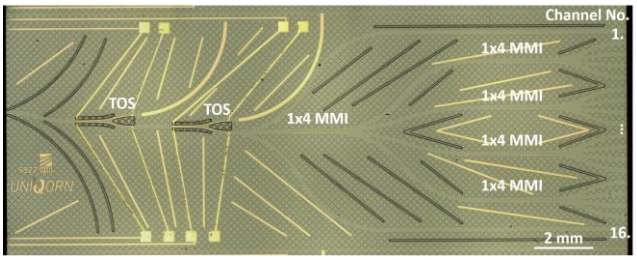

Fig. 1. Fabricated 1:16 QRNG PolyBoard. The chip comprises two cascaded thermo-optical switches (TOSs) and four 1x4 MMIs to achieve the 1:16 splitting.

A. Single Photon Avalanche Diodes

SPADs are quite appealing for implementing an integrated QRNG. They provide single photon sensitivity, allow the possibility to embed smart electronics on the same chip, thus reducing external processing, and can be integrated with photonic platforms. We designed and manufactured a SPAD chip consisting of a linear array of 32 SPAD pixels, with 125 µm pitch; every pixel contains 4 different SPADs with 5 µm, 10 µm, 20 µm and 50 µm diameter, respectively, so as to easily match different waveguide dimensions and optical systems.

A microphotograph of the 32-pixel SPAD chip is reported in Fig. 2. The chip provides 32 independent outputs, one per pixel, with a digital pulse for each detected photon, that can feed external counters (for photon counting applications) or time-measurement electronics (such as TTMs, for photon "timing" and Time-Correlated Single Photon Counting applications). Furthermore, for the specific QRNG application, the chip performs on-chip photon coincidence detection in two modalities: single-hit and multi-hit. The former provides a digital pulse only when one photon is detected by the array within a programmable time window, while discarding all other events with two or more photons; also, the 5-bit address (from pixel 0 to pixel 31) of the only triggered pixel is provided. In this way, when a randomly routed photon is detected by the array, such an address directly gives the random code. The latter modality allows to provide a digital pulse only when at least an N-photon (N is user-selectable among 2, 3, and 4 photons) coincidence event is detected. For both modalities, the coincidence time-window can be programmed from 1 ns to 24 ns.

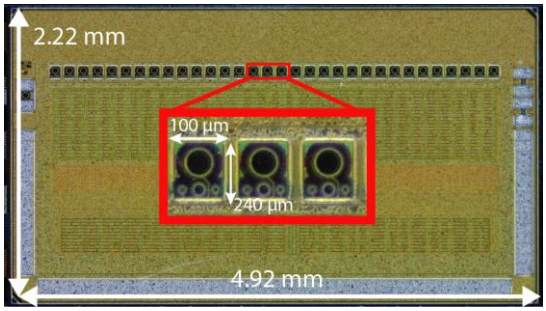

Fig. 2. Microphotograph of the 32-pixel SPAD chip, with a zoom-in showing the 4 SPADs in each pixel.

We characterized the SPAD chip performances. The photon detection probability (PDP) shows a peak at 500 nm wavelength in the 45% – 65% range. Such variability is due to edge effects, at the border of active area, which lower the detection efficiency above all for smaller diameter SPADs. The dark count rate (DCR) and timing jitter are 45 cps (counts per second) and 28 ps for the smallest SPADs, while 8.6 kcps and 60 ps for the largest ones. The afterpulsing is kept below 0.3%.

B. QRNG characterization

An external pulsed laser source at 795nm was coupled to the QRNG chip for randomness generation. The two TOS were used to attenuate the photon pulses down to single-photon level. The passive splitting loss of the two TOS is 6 dB. The total extinction ratio was measured to be 6 dB. To achieve the single-photon regime, the two TOSs are used in combination with an external VOA (variable optical attenuator). Light is split via a 1x4 MMI section into four optical modes. Four external Si-SPADs are coupled to the polymer waveguides and connected to the Time Tagging Module (TTM), TTM8000, for data analysis. Upon detection events, binary packets are created, each composed by detection time and channel number, and sent from the TTM to the postprocessing. The postprocessing routine involves the conversion of the binary data packets to event data, pulse detection to minimize the influences of afterpulsing effects and event filtering to guarantee the availability of all 4 detectors for entropy gathering via disabling event processing during the detector deadtime. The QRNG generates one of 16 output states or 4 bits of raw random numbers per photon pulse. The theoretical upper limit for randomness generation is set by the deadtime of the detectors used. For silicon SPADs this is typically tens of ns [6]. To classify the amount of uncorrelated and uniformly distributed randomness in the raw numbers, a min-entropy calculation is performed (adjusted from [7]). This considers the detector efficiency, splitting distribution, dark-counts and input photon number. The Toeplitz hashing algorithm [8] was used as a randomness extractor resulting in a uniformly distributed and uncorrelated random number string passing all 15 NIST tests [9] used for classifying random numbers. Experimentally, the laser was attenuated at the single-photon level and a 1 MHz repetition rate was chosen. This can be increased in principle up to the inverse of the detector deadtime to generate higher raw bitrates. In our case, however, the limiting factor was set by the TTM processing speed.

For a 1 MHz pulsed laser frequency, a raw random bit rate of 3.7 Mbit/s was obtained. The randomness extraction then reduces the raw random bitrate according to the min-entropy which is at around 0.68 for the optimized settings. This means that ~68% of the raw random bitrate can be extracted to generate an uncorrelated uniformly distributed bitstream.

Existing QRNG bitrates range from hundreds of kbps to around a few Gbps, which places this first generation QRNG module already at an excellent level, and room for further improvements on the integration side and generated bit rate in the future.

C. QRNG module with integrated SPADs

The QRNG assembly required a fully customized packaging approach, developed by Cordon Electronics. In this application, the two chips of the system, the PolyBoard PIC and the SPAD electronic application specific integrated circuit (ASIC), need to be mounted together perpendicularly to maximize the coupling efficiency. The packaged module must be robust against mechanical stress to ease the handling during operation. The package structure thus is made of two main building blocks: the vertical subassembly with the PolyBoard chip and the horizontal printed circuit board (PCB) hosting the SPAD chip. The two parts are assembled separately and merged at the end of the packaging procedure.

The first part of the system houses the PIC, and everything needed to provide optical and electrical access to it. The chip is placed on an insulating aluminum nitride submount. The optical signal is provided to the PIC with a single pigtailed fiber that is aligned to the chip input and then glued to it. The mechanical stability of the fiber is improved with spacers mounted on the submount. The second part of the package is the horizontal two-layer PCB with the electronic ASIC. In addition to housing the co-packaged chips, the board has an edge connector on one side, that is used to plug the assembled module into a custom breakout PCB providing all the electrical signals needed to operate the QRNG module. The many electrical tracks are routed from the ASIC to the edge connector in two steps. The chip is first wire-bonded to a two-layer electrical interposer, to match the pad's pitch to that of the PCB. A second layer of bondings then connects the interposer to the PCB, on which the signals are routed to the connector.

Eventually, the two assembled halves of the module are merged. To do this, the polyboard subpart needs to be optically aligned to the SPAD chip. Active optical alignment has been performed using the detectors on the ASIC. A custom board specifically designed to convert their signal into a readable current has been used to facilitate the alignment procedure. Optical glue between the two chips is used to minimize the coupling losses. The final assembled module is shown in Fig. 3(a). To increase the mechanical robustness of the package two strategies have been used. First, reinforcement stubs have been placed at the junction between the PCB and the vertical submount. In this way, misalignment of the chips is avoided. In addition, a custom plastic cover has been 3D printed to protect the chips and wirebondings from damage, as shown in Fig. 3(b). This is required if the module has to be safely handled in a laboratory environment.

The finalized packaged device is a 1x16 QRNG Module, equipped with an integrated array of 16 SPAD. Dark-count rates, insertion losses and detector efficiencies were characterized. Dark-count rate measurements showed count rates below 30c/s for the highest bias voltage of 31V and count rates below 5c/s for a bias voltage of 27V. The dark-count rates compare well with commercial bulk Si SPAD modules [6], especially since the SPAD array of the QRNG chip operates at room temperature. The dark-count rates compare well with commercial bulk Si SPAD modules [6], especially since the SPAD array of the QRNG chip operates at room temperature. A 795nm external laser was used for the detection efficiency estimations. The bias voltage was tuned in the range (28-30) V. Total insertion losses for the different channels range from around -26.8 dB to around -29.6 dB.

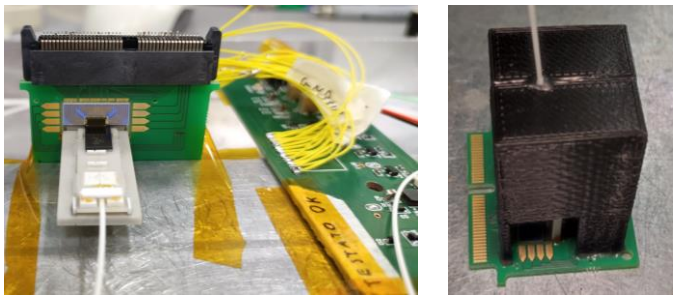

(a) (b)

Fig. 3. (a) Fully assembled QRNG system. (b) For protection during experimental trials, a 3D printed plastic cover is glued to the PCB.

These losses include fiber coupling to waveguide (1.5dB), waveguide propagation loss (2 dB), 1x16 splitting loss (12 dB), passive TOS attenuation (6 dB) and coupling of the waveguides to the SPADs. Ideally the coupling waveguides to SPADs is almost lossless (because the active area of the SPADs is larger than the waveguides). The excess losses are probably attributed to the module assembly.

Detector efficiency measurements for 3 bias voltages (28, 29, 30) V showed an average efficiency of 5,9%, 7,7% and 8,8% respectively, which increases due to the improved triggering probability at higher "excess voltage" above breakdown. These agree with the direct detector efficiency characterization before packaging (about 14% at 800nm). Raw random bit estimations and randomness extraction are ongoing and will be reported soon.

III. InP INTEGRATED QKD TRANSMITTER

An integrated QKD transmitter was designed and fabricated with the goal of generating pulse trains of weak coherent states [10,11]. The functional schematic of the transmitter is shown in Fig. 4(a). Various active and passive components have been monolithically integrated to realize a transmitter capable of generating optical pulses while carefully controlling the number of photons per pulse, as well as providing phase and amplitude encoding. A distributed Bragg reflector (DBR) laser [12], consisting of a semiconductor optical amplifier (SOA) and a phase modulator section in a cavity of two DBR mirrors, is employed as the light source. The intracavity phase modulator provides fine-tuning of the cavity length and therefore precise control of the laser emission wavelength. The photodiode (PD) outside the cavity allows monitoring the optical power of the laser. The laser is followed by an electro-refractive phase modulator to control and encode the phase of the continuous signal from the laser. The pulse carver, which is designed as a Mach-Zehnder modulator (MZM) with electro-refractive modulators (ERM) in each of the interferometer arms provides the pulse formation and mitigates the transition effects. The modulated and encoded signal is then passed through a variable optical attenuator (VOA) to achieve the required output level. Two different ways of attenuation are used in the transmitter, one consisting of a 3-stage Mach-Zehnder interferometer (MZI) and one consisting of a 3-stage SOA-based attenuator.

Fig. 4(b) shows a microscope image of the transmitter, fabricated in the generic InP multi-project-wafer platform of Smart Photonics [13,14]. The fabricated transmitter was then packaged by Cordon Electronics in a gold-box package [15]. The packaging of a single chip with optical access and electrical connections was required. Both low frequency and RF electrical signals needed to be brought to the photonic chip (PIC). The medium complexity of the assembly allowed to follow the "gold box" packaging approach, where the chip is mounted inside a standard metal package having the suitable optical and electrical connectors. The package used for the assembly is a standard kovar package with dimensions 50 x 35 x 8.6 mm, having the DC pins on the north and south sides, the RF connectors on the west and the optical inputs/outputs on the east.

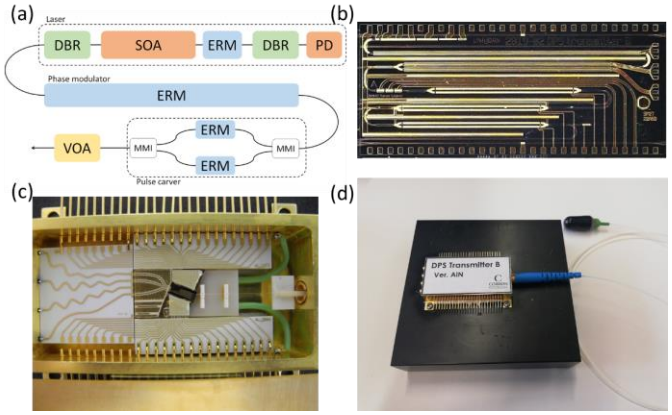

Fig. 4. (a) Schematic of the QKD transmitter (b) Microscope image of the fabricated chip (c) Image of the chip mounted on the interposer (d) The final packaged transmitter module.

The internal structure of the package is shown in Fig. 4(c). The photonic chip is mounted in an angled position, to account for the refraction that light experiences when passing from the AR-coated angled integrated waveguide to the lensed optical fibers. This approach allows to minimize the internal reflections of the chip and maximize the coupling with the fibers, resulting in minimum coupling losses.

The optical fiber attachment is glued to suitable spacers for alignment and is secured in the gold-box feed through, which also absorbs the mechanical stress when handling the packaged module. The access to the north-south DC pads of the PIC is obtained by using two thick-film alumina interposers made of two parts each. A standard interposer provides the first part of the routing from the DC connectors to close to the chip, to fanout from the PIC pads pitch to the DC pins pitch. A second customized part brings the electrical signals to the PIC, matching the position of the pads to ensure that short and reliable wire-bonding and all the electrical connections can be done. The same approach is adopted for the connection of the RF signals. In this case, a thin-film alumina interposer is used for the first part of the routing from the GPPO standard connectors. The use of a thin-film alumina is more suitable for RF signals than the thick-film used for the DC tracks. The final part of the routing is instead done with a custom interposer, that allows to design thin tracks, required to match the PIC pads pitch, while keeping impedance matching. Signals at up to 40 GHz can be routed in this way. The thermal management of the PIC is obtained thanks to a thermoelectric cooler (TEC) and a thermistor, both housed

inside the package. The TEC is glued with a thermally conductive paste to the package bottom to remove the heat generated in the system. A custom CuW submount is glued on the other side of the TEC, to electrically isolate it from the PIC. This is for vertically aligning the PIC to the electrical interposers and to hold the optical fiber in place with the spacers. The cold side temperature is sensed with a thermistor mounted on the CuW submount close to the PIC, that is read through the DC pins of the package. Since both the PIC and the optical fibers are attached to the cold side of the TEC, thermal expansion does not stress the optical alignment. Fig. 4 (d) shows the final packaged module.

A. QKD transmitter characterization

Fig. 5(a) depicts the LIV characteristics of the laser, where the optical output power is measured using the monitoring PD, which typically has a responsivity of 0.8A/W. The threshold current of the laser is around 32mA. The resulting optical spectrum, while the laser is being operated at 44mA, is measured from the optical output port of the chip and is shown in Fig. 5(b). The spectrum shows a single mode emission around 1550nm with >55dB side-mode-suppression ratio. Two neighbouring peaks around the main mode result from a relaxation oscillation frequency of around 3 GHz. At the same laser current, the instantaneous linewidth is measured to be around 2 MHz using OEWaves OE4000 phase noise and linewidth measurement system.

Fig. 6(a) shows the DC response of the pulse carver. The extinction ratio is over 20dB, and 4V is needed to obtain π phase shift.

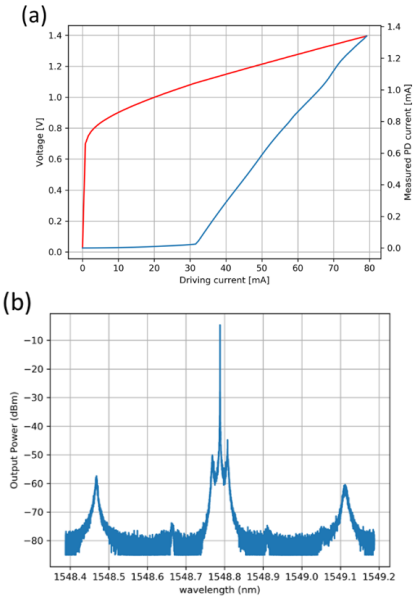

Fig. 5. (a) LIV characteristics of the DBR laser, and (b) output optical spectrum at 44mA laser current.

Fig. 6(b) shows the corresponding scattering parameter (S_{21}), where the 3-dB cut off point is measured to be around 590MHz. The pulse carver functionality is further examined by driving one of the MZM arms with a 1kHz pulse-shaped electrical signal with a peak-to-peak voltage of 2.3V around -3V DC bias, while the optical output from the chip is attenuated to the single photon level. The resulting signal is used as the input to a commercial single-photon avalanche diode (SPAD). Fig. 7 depicts photon count rates at different drive voltage levels. The extinction ratio between two levels is calculated as 11.1 dB using the formula,

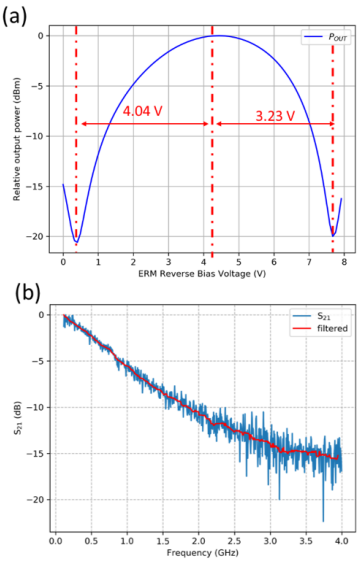

Fig. 6. (a) The DC response and (b) the dynamic response of the pulse carver.

$$ER = 10\log_{10}\left(\left(\frac{N_{high}-R_dT}{N_{low}-R_dT}\right)\frac{1}{\eta_{dead}}\right),$$

where the N_{high} and N_{low} are respective photon counts at the high and low drive voltage levels, R_d is the dark count rate of the SPAD which is 500 counts per second in this case, T is the duration of the signal where it is high or low, which is half the signal period in this case, and η_{dead} is the term which accounts for the dead time of the SPAD [16] and calculated to be 0.55. The response of the single-stage MZI-based, and SOA-based VOAs was characterized.

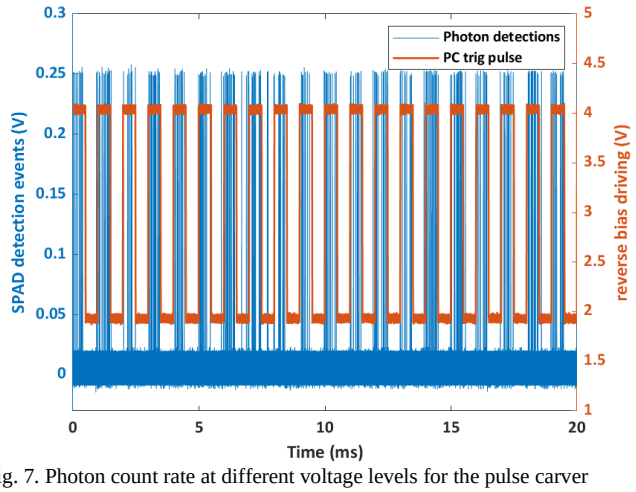

Fig. 7. Photon count rate at different voltage levels for the pulse carver

The MZI-based VOA can achieve around 25 dB of extinction ratio with a 5.4V voltage difference, whereas the SOA based VOA can achieve up to 10 dB of extinction ratio with a voltage difference of around 8V.

B. COW protocol demonstration with QKD transmitter

Quantum key distribution allows the exchange of secure keys between two parties, commonly called Alice and Bob. The

underlying principle of QKD is that nature prohibits to gain information on the state of a quantum system without disturbing it. Since the initial proposal of the BB84 protocol back in 1984 [17], QKD has become a mature quantum technology, highlighted by the already impressive QKD networks demonstrated so far [18,19]. Among the different QKD protocols proposed so far, the COW protocol is particularly suited to practical implementations [20]. COW QKD uses a simple state preparation and symbol encoding scheme, as depicted in Fig. 8. Alice generates a stream of weak light pulses located at equidistant time slots and maintaining a constant relative phase φ between neighboring pulses. Within this coherent train, every pair of time slots corresponds to a sent symbol: a key symbol "0" is encoded by an occupied *early* timeslot, whereas a key symbol "1" has the *late* timeslot of the pair occupied. To guarantee the safety of the protocol, Alice additionally prepares so-called decoy states at random with both slots of a pair occupied. Because of this 1:2 relationship between symbols and pulse slots, the source symbol rate is always half of the fundamental pulse rate of the transmitter.

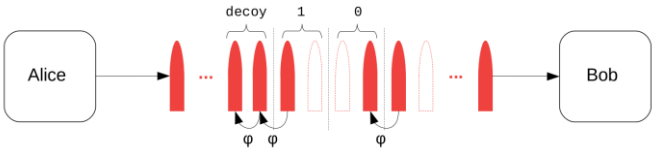

Fig. 8. Symbol encoding scheme used in the COW QKD protocol.

The performances of the QKD transmitter, which was designed as a differential phase shift (DPS) transmitter have been investigated [21]. The chip was tested in a bulk COW QKD setup where the generated optical pattern was sent to an existing QKD receiver as depicted in Fig. 9.

The COW receiver comprises a 75:25 splitter which divides the signal into a data and monitoring channel. The data channel which is at the 75% output, carries the QKD pattern to a SPAD where it is detected and subsequently sent to postprocessing.

The monitoring channel consists of a MZI which is used to detect a potential eavesdropper. The dark output port is monitored with a SPAD to detect any deviation of the photon counts.

Characterization measurements for an initial estimation of visiblity, extinction and stability were performed. For the stability, the generated light signal was set to CW (continuous wave) and the dark output port of the MZI was recorded for almost 2 hours. A stable output for around 1 hour and 10 minutes within a threshold of around 400c/s was recorded. Extinction-ratio measurements were thoroughly investigated for optimizing the visibility of the QKD pattern. For this, a pattern of alternating ones and zeros was input and the received pattern was used which resulted in a value of around 15 dB, close to the preliminar characterization reported in Fig. 7. The visibility measurement was performed via measuring the dark and light ouput port of the MZI with a resulting visibility of 0.964 with a negligible measurement error due to the long measurement time.

A COW QKD run was performed via connecting the integrated transmitter to the QKD receiver as shown in Fig. 9. The photon number per pulse was adjusted via the VOA at the 99:1 splitter output, to a value of 0.1 photons per pulse.

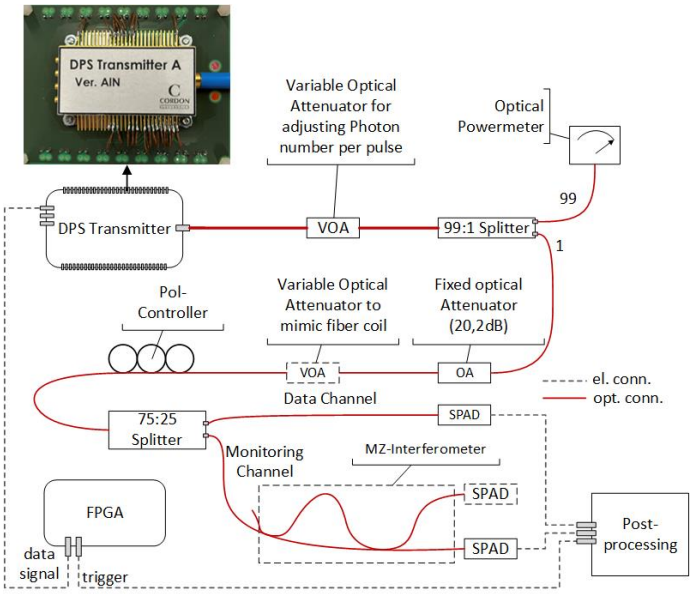

Fig. 9. Block diagram of the COW QKD setup and photograph of the DPS transmitter. The optical pulse train generated by the transmitter is sent via an optical fiber to a variable optical attenuator (VOA) where the photon number per pulse can be adjusted. After the VOA a 99:1 splitter divides the optical signal towards an optical powermeter and the quantum channel to the receiver. The 1% output is connected to a fixed optical attenuator to decrease the optical signal to quantum level. A subsequent VOA is used to mimic transmission losses of a fiber coil, a polarization-controller adjusts the polarization of the signal for the MZI of the receiver.

The transmitter generated a random number pattern of 64 bits of 1ns length each. This 64 ns long pattern was repeated with a frequency of 500kHz. The pattern was recorded with the sender and receiver in a back-to-back (0 km fiber, 0 dB additional attenuation) configuration and with the variable optical attenuator mimicking a fiber coil at 3 dB and 6 dB. Calculated QBER was 0.019 for back-to-back and 0.017 for 3dB and 6dB additional attenuation. The raw key rate for back-to-back sending resulted to be 6198 bps, 4159 bps for 3 dB attenuation and 2539 bps for 6 dB attenuation.

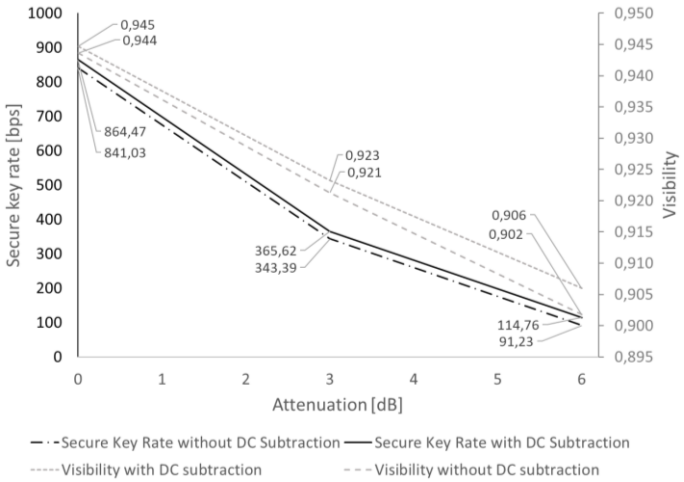

Fig. 10. Computed secure key rates with and without dark-count subtraction are shown in black, left vertical axis. The measured visibilities with and without dark-count subtraction are shown in gray, right axis.

The secure key rate and the visibility for the three attenuation settings is shown in the Fig.10. The analysis is performed both without and with subtraction of the dark-count rate, which minimally increased the visibility. Compared to our existing COW system based on bulk components, the transmitter exhibits a lower visibility with a difference of around 5% and a higher QBER with a difference of around 1%. This is likely related to the relatively strong sidemodes of the QKD transmitter. The side-modes are related to mode-hopping of the integrated laser, which induce phase noise in the MZI, limiting the visibility, and, in turn, the secure key rate. Improved next generation QKD transmitter chips are in production and will be characterized and tested soon.

IV. LOW-NOISE INTEGRATED QKD RECEIVER

Quantum key distribution protocols come in many different flavors. One of the main distinctions is the use of discrete variable (DV) or continuous variable (CV) encoding. Whereas DV protocols have been studied for longer and possess more mature security proofs, their reliance on single photon detection presents still a hurdle. Single photon detectors in the near infrared are either based on SPADs or superconducting nanowires with both types possessing practical limitations in terms of efficiency and operational complexity (cryogenics) respectively [22]. Here CV-QKD has an advantage since the detection unit is based on balanced homodyne detectors which feature in principle high bandwidth and high efficiency and can be more easily integrated on chip. Since the main contribution to the error in CV-QKD comes from the noise of the receiver unit [23], it is paramount to reduce its intrinsic noise.

A. *QKD receiver design*

For a CV-QKD receiver, a low-noise transimpedance amplifier (TIA) is used to convert the weak differential current produced by the balanced photodetectors to a sufficient level for processing, without distorting the signal or adding much noise. TIAs in earlier balanced detectors have usually been constructed by using discrete off-the-shelf components [24] or a commercial bare die TIA used in telecom applications [25]. This results in a CV receiver having low bandwidth or poor noise/linearity, causing severe distortion. Linear commercial TIAs do exist, but are usually for high baud rate, long-reach coherent applications and would be too noisy for quantum communications.

Within the UNIQORN project, a TIA with a bandwidth in excess of 1 GHz, linear operation, and ultralow noise performance was targeted [26]. While silicon metal–oxide–semiconductor field-effect transistor (MOSFET) technologies exist in very small nodes with a high transition frequency f_t, they have been shown to suffer from poor noise performance for small channel lengths [27]. High electron mobility transistors (HEMTs) are another type of FET that use III-V materials such as GaAs, GaN, or InP. Compared to silicon, these III-V materials achieve improved electron mobility and a higher saturation velocity, which yields high speed and low-noise devices [28]. In this work, a 100 nm GaAs pseudomorphic HEMT (pHEMT) technology is used with a typical f_t of 130 GHz. As shown in Fig. 11, the TIA consists of a three-stage amplifier and an output buffer. Each stage is composed by a common source amplifier followed by a source follower with a level-shifting Schottky diode and current source. A 50Ω buffer is added to isolate the TIA core from any outside loading and to provide 50Ω matching toward measurement equipment. A detailed framework for modelling and optimizing the circuit noises of the low-noise TIA can be found in [26].

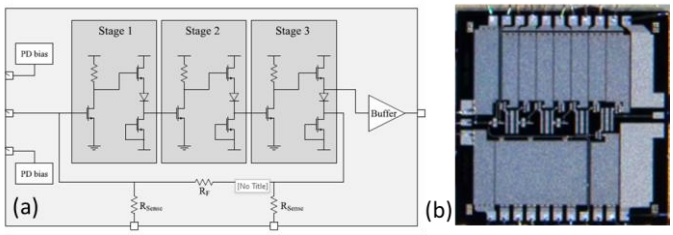

Fig. 11. (a) Schematic of the transimpedance amplifier circuit. (b) Micrograph of the manufactured pHEMT TIA chip.

B. *Characterization of low-noise transimpedance amplifier*

The frequency response of the fabricated TIA was measured with a silicon PIC [26] using an Agilent N5247B PNA-X network analyzer. The full two-port S-parameters are measured and the response of the external modulator was calibrated out first. The S_{21} transmission coefficient of the calibrated S-parameters is used to measure the transimpedance gain, which can be seen in Fig. 12. A 3-dB bandwidth of 1.5 GHz is obtained. The output matching parameter S_{22} is also shown and is less than -10 dB below 10 GHz. This guarantees very little reflections in the frequency band of operation when connecting the TIA with other 50Ω devices after the CV receiver.

A common figure-of-merit for balanced receivers is the quantum shot noise to classical noise ratio, commonly referred to as clearance [23]. A large amount of clearance enables longer reach communications in CV-QKD and guarantees low overhead in QRNG, increasing the maximum random number generation rate.

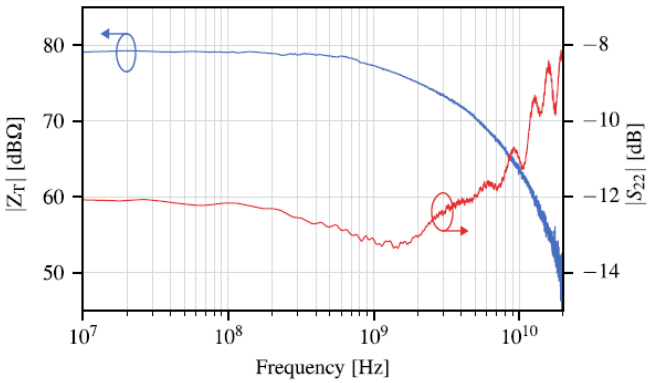

Fig. 12. Measured transimpedance gain and output matching parameter (S_{22}).

The clearance can be written as Eq. 1. It is shown clearly that for realizing high levels of clearance it is essential that the TIA has a low input referred current noise density (IRND, $I^2_{n,TIA}$), which consists of noise components from various devices as shown in Eq. 2. The noise contributed by the feedback resistor RF has a white spectrum and is the dominant source of noise at low frequencies. At high frequencies the transistor drain noise becomes the dominant noise source. The 1/ f noise is not taken

into account because this should have a minimal effect, considering the frequency range of interest.

$$\text{Clearance} = 10\log_{10}\left(\frac{I_{n,\text{shot}}^2}{I_{n,\text{clas}}^2}\right)\text{[dB]}$$

$$= 10\log_{10}\left(\frac{2q\overline{I_{\text{PD,bot}}} + 2q\overline{I_{\text{PD,top}}}}{I_{n,\text{TIA}}^2}\right)\text{[dB]}. \quad (1)$$

$$I_{n,\text{TIA}}^2 = \underbrace{\frac{4kT}{R_F}}_{\text{Contribution R}_F} + \underbrace{2qI_G + 4kT\Gamma\frac{(2\pi C_{\text{in}})^2}{g_m}f^2}_{\text{Contribution Q}_1} + \ldots, \quad (2)$$

To calculate the clearance, we constructed Fig. 13 by plotting the power spectral density (PSD) for a single frequency (f=100 MHz) versus the current. For low currents (i.e., low levels of shot noise), the noise is dominated by the electrical background noise.

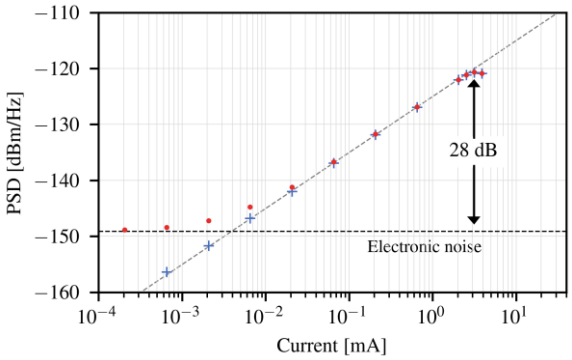

Fig. 13. Power spectral density (PSD, marked by the red dots) measured at 100 MHz for different photocurrents flowing through the photodiodes. A maximum of 28 dB clearance between the electrical noise caused by the TIA and the shot noise is obtained at this frequency. The blue crosses represent the PSD with the electronic noise removed, demonstrating the increase in shot noise when the photocurrent rises.

This background noise is obtained separately by blocking both optical input ports. As the current increases the shot noise becomes the dominant source of noise. A maximum shot noise to electrical noise clearance of 28 dB is measured at 100 MHz for a current of 3.14 mA. Compared to previously published works [24-25, 29-30], the TIA in this work is able to achieve a high bandwidth while at the same time improving significantly in terms of noise.

C. Balanced receiver: design and packaging

The schematic diagram and the picture of the fabricated InP balanced receiver chip is shown in Fig. 14. The chip includes an on-chip local oscillator (LO), a multi-mode interference (MMI) based 90° hybrid coupler, and two balanced detector pairs. In-phase and quadrature signals provide the current output from the chip, which are to be fed into their respective trans-impedance amplifiers. A MMI based 1×2 coupler is used to support operation either with the on-chip LO or an external LO.

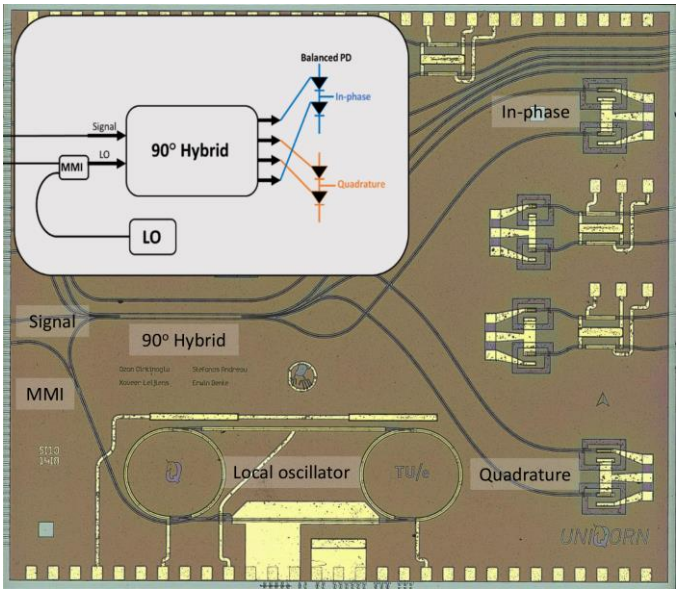

Fig. 14. Photograph of the InP balanced receiver PIC with on-chip local oscillator, 90° hybrid and balanced photodetector pairs. The inset shows the receiver schematic.

A uni-directional Vernier ring laser is utilized as the local oscillator [31]. The laser exhibits linewidths down to 50 kHz and emits single-mode output across 1540 nm and 1570 nm. The output spectrum of the laser under a bias current of 102 mA is reported in Fig. 15.

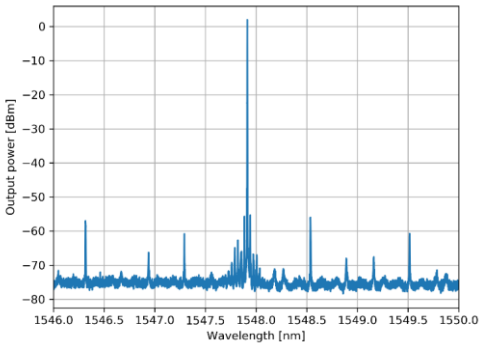

Fig. 15. Output spectrum of the local oscillator laser

It shows single-mode emission around 1548 nm with a side-mode-suppression-ratio (SMSR) of around 60 dB. The 90° hybrid has a common-mode rejection rate (CMRR) of below -25 dB across a 5 nm range, and below -20 dB across a 10 nm range around the center wavelength of 1550 nm [32].

The balanced receiver module comprises of 3 chips that need to be packaged together. Since a proper RF routing is required, the chips are mounted on a custom 85 mm x 70 mm PCB, that provides all the electrical connections to operate the system, and optical access is achieved with a couple of optical fibers. The PIC is placed close to the PCB edge to facilitate the optical coupling and the two TIAs are glued very close to it to minimize the length of the RF wire-bondings. The PCB hosts also the decoupling capacitors needed to operate the two-application specific integrated circuit (ASICs) and the RF and DC connectors to provide and read all the electrical signals. The optical coupling is done by using two optical fibers, that are

required for the local oscillator and receiver signals. A cavity of around 0.7 mm depth has been opened in the PCB, as shown in Fig. 16(a) to directly edge-couple the fibers to the chip. Mechanical stability is obtained by placing properly shaped spacers below the fiber.

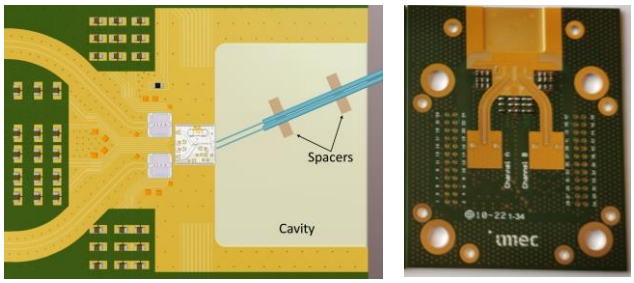

(a) (b)

Fig. 16. (a) Detail of the optical coupling: a vertical cavity opened in the PCB to accommodate the fibers. Spacers hold the fibers in place and increase the mechanical reliability. (b) Packaged balanced QKD receiver.

The electrical connections to all the chips have been realized with wire-bondings. To correctly route all the RF signals, the ASICs position has been studied to minimize the length of the connections to the PDs. The layout of the PCB has been designed after proper RF simulations to ensure impedance matching and correct signal bandwidth. SMA connectors were chosen to connect the RF outputs of the module to external instrumentation.

The DC connections are required both to operate the ASICs, providing the power supplies and low frequency control signals, and to drive the PIC. The ASICs have been directly wire-bonded to the PCB. The PIC is firstly connected to an interface aluminum nitride interposer, that provides fanout of the connections while a second set of wire-bondings then connects the interposer to the PCB. This approach allows maximum flexibility in the connections, making the PCB suitable to operate both the balanced and the homodyne receiver PIC with the same design. Thermal management of the module is obtained with a Peltier thermo-electric cooler glued below the PCB with thermally conductive paste. Proper thermal connection is ensured by placing vias between the chips and the TEC, that allow efficient heat transfer. The average temperature of the assembly is monitored with a thermistor soldered close the chips. The final packaged chip is shown in Fig. 16(b).

V. NON-CLASSICAL PHOTON SOURCES

The development of efficient integrated non-classical photon sources is of paramount importance for quantum communication applications, in particular for QKD. While strongly attenuated lasers, thanks to the ease of operation, are often used for generating single photons, heralded photon sources typically show advantages in terms of secret key rate and security, due to the suppressed probability of multi-photon events. Entangled photon sources, on the other side, provide inherent source-independent security. In addition, entangled photon sources can be employed in several other quantum applications such as quantum sensing (e.g. ghost imaging), quantum computing (e.g. photonic cluster states) and in quantum repeater links.

Apart from the fabrication of QRNGs outlined in Section II, the PolyBoard photonic integration platform also enables the hybrid integration of nonlinear materials, that create photon pair sources via spontaneous parametric down-conversion (SPDC). Within the UNIQORN project, the integration of periodically poled lithium niobate (ppLN) waveguides, Bragg-reflector waveguides (BRWs) and periodically poled potassium titanyl (ppKTP) bulk crystals was demonstrated. The first two nonlinear waveguides are butt-coupled to polymer waveguides, the latter is integrated inside an on-chip free-space section created by two GRIN-lenses. Additionally, the PolyBoards include long-pass thin-film filters (LP-TFF) for pump suppression, dichroic mirrors (DM) and polarization beam splitters (PBS) for separation of signal and idler photons. Precisely etched U-grooves inside the polymer enable the coupling of single-mode fibers for further processing of the separated photon pairs.

A. *Heralded photon source*

A SPDC-process in a Ti-diffused ppLN waveguide, pumped at 532nm, generates photon pairs at 810nm (signal) and 1550nm (idler). Detection of the signal photon is used to herald the idler single photon. The ppLN waveguide is coupled in input to the 532nm pump via U-groove. The waveguide output is coupled to PolyBoard waveguides, which include long pass filters (LP) for pump suppression and dichroic mirrors (DM) for signal and idler separation into two output fibers as shown in Fig. 17. The DM provides a suppression > 30 dB and losses of 0.5 dB for 810 nm in the reflected path and of 1.5 dB for 1500 nm in transmitted path.

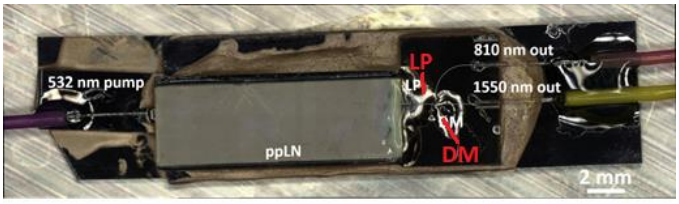

Fig. 17. Assembled heralded photon source consisting of a ppLN-waveguide coupled to an input and output PolyBoard, with long-pass thin-film filter (LP-TFF), dichroic mirror thin-film element (DM-TFE) and in/out fibers.

The ppLN waveguide can be heated for phase-matching tuning and the end-facets are coated to ensure high transmission between the crystal and PolyBoard. The coupling losses between the waveguides on PolyBoard and ppLN were measured to be 1.0 dB. Full integration of all components leads to a compact, mm-sized heralded single photon source. We measured the spectra of both output ports and calculated the heralding efficiency η_h as well as the heralded second-order auto-correlation $g^2_h(0)$ from coincidence measurements [33]. Fig. 18(a) shows the output spectrum of signal output port at T=30°C. The PDC peak is clearly visible at around 825nm.

In Fig. 18(b) the calculated heralded efficiency as a function of the input pump power is reported. For low pump powers, a heralding efficiency of around 3.5% and $g^2_h(0) < 0.05$ can be achieved, which indicates a high single photon character. With an improvement of the coupling efficiency between ppLN waveguide and PolyBoard, we expect a significant increase of the heralding efficiency and improved overall performance.

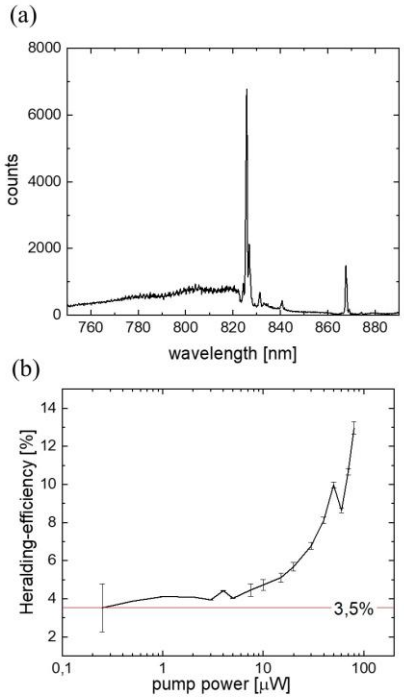

Fig. 18. (a) Spectrum at the signal output port at T=30°C and (b) heralding efficiency versus pump power

B. *Polarization-entangled photon source*

A double SPDC process in a ppKTP crystal with pump light at 515nm light is excited, yielding a pair of polarization-entangled and color-entangled photons. One photon is emitted at around 1500nm, while its orthogonally polarized counterpart is emitted around 785nm. The classical transmission loss through loss the similar on-chip free-space sections of the same length is typically 2 dB. A bulk experimental demonstration of a similar entanglement design was demonstrated in [34]. As shown in Fig. 19, the crystal is placed on a Peltier element of a Polyboard, whose guided section also includes a dichroic mirror to separate the two photons with a suppression > 30 dB. The losses for 785 nm in the reflected path are 0.5 dB and for 1500 nm in transmitted path around 1.5 dB.

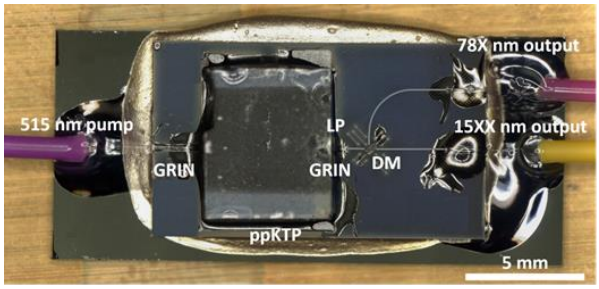

Fig. 19. Assembled entangled photon source consisting of a ppKTP crystal integrated with an on-chip free-space section created by two GRIN-lenses. with long-pass thin-film filter (LP-TFF), dichroic mirror thin-film element (DM-TFE) and in/out fibers.

The temperature can be actively tuned with an externally connected temperature controller to find the crystal's phase matching condition. Spectra have been recorded thoroughly and analysed with single-photon spectrometers at NIR and telecom wavelengths. Under careful optical design, the two centre wavelengths of one SPDC pair can be brought to coincide with those of the respective counterparts of the other, orthogonally polarised, pair. In this configuration, the two SPDC processes are indistinguishable resulting in the emission of bipartite entangled photons. An exemplary characterization measurement is reported in Fig. 20.

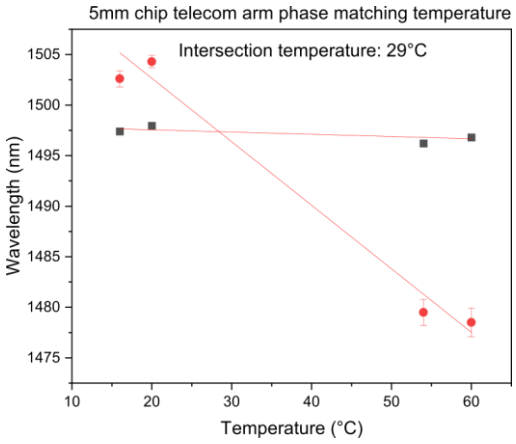

Fig. 20. The spectra of both SPDC processes are recorded and fitted for a range of temperatures. SPDC central wavelengths are plotted against temperature. The phase matching temperature is the one for which the centre wavelengths of both processes intersect, resulting in the emission of polarization and colour entangled photons.

After the generation process, the photons are transmitted through an integrated long pass filter, separated by an on-chip dichroic mirror and eventually coupled to two optical fibers via GRIN lenses. The 785 nm photons were detected using silicon SPADs, with efficiency around 60 %, while the 1550 nm photons were detected using InGaAs SPADs, with efficiencies around 20 % (deadtime 10 μs). Measured singles for an input pump power of 5mW at the operational temperature of about 29°C are 45 kHz in the visible and 18 kHz at telecom. Coincidence rates of up to 110 Hz were reached without any spectral filtering, with a coincidence-to-accidental ratio (CAR) of 24. The measured coincidence rate and CAR are understood to be limited by spurious fluorescence signal around 785nm generated by the glue employed in packaging the chip. New generation chips were produced with negligible fluorescence at the operational wavelengths. The quality of the generated quantum polarization correlations is currently under investigation and will be reported soon.

C. *Time-bin entangled photon source*

Time-bin entanglement encodes the quantum information into superpositions of a photon being in an earlier or later time slot. AlGaAs Bragg-reflection waveguides (BRW) can be used as miniature sources of time-bin entanglement [35]. However, so far there are no BRW chips that include the required passive optical elements such as filters, splitters, and polarization optics. All of these elements can be hybrid-integrated on PolyBoard chips, which also couple better to fibres.
The entanglement creation chip consists of a BRW chip end-face coupled to a PolyBoard and glued to a carrier as shown in Fig. 21. The mismatch of the symmetric mode field in the

PolyBoard and the asymmetric mode filed in the BRW yields a coupling loss of 2.7 dB between both waveguides.

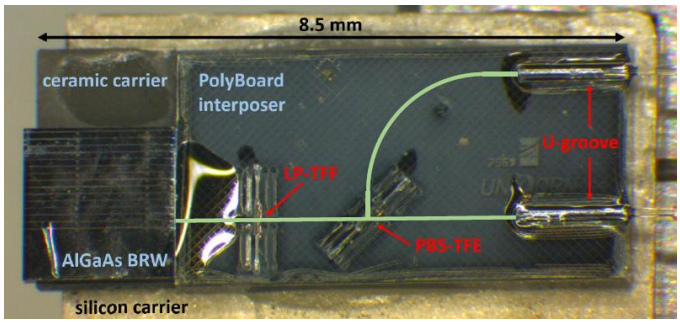

Fig. 21. Assembled photon pair source fixed on a submount with long-pass thin-film filter (LP-TFF) and a polarizing beam-splitter thin-film element (PBS-TFE).

The coupling between the BRW and the PolyBoard waveguide is optimized for second harmonic signal. On the PolyBoard interposer there is a long-pass thin-film filter (LP-TFF) to remove any remaining pump light. The on-chip suppression of the 775 nm pump light in the waveguide was measured to be 68 dB. The photon pair is split at a polarizing beam-splitter thin-film element (PBS-TFE) where TE-polarized light is transmitted with 1.2 dB loss, and TM-polarized light is reflected with 0.5 dB loss. The polarization extinction ratio of these filters is in excess of 45 dB for 1550 nm and 25 dB across the C band. Fibre coupling is achieved via U-grooves.

We tested the nonlinearity of the entanglement generation chip by pumping parametric down-conversion in the BRW with a NIR pump laser with a period of 13 ns. The coincidence signal between the two orthogonally polarized telecom photons is shown in Fig. 22. The central peak corresponds to true coincidences, while the side peaks are accidental coincidences at a distance equal to the period of the pump laser.

The full time-bin entanglement scheme involves a free-space interferometer in the pump path that is used to split pulses into pairs of pulses with 200 ps delay. To analyze the time-bins, we employ PolyBoard chips with asymmetric Mach-Zehnder interferometers (aMZIs) with the same delay, shown in Fig. 23.

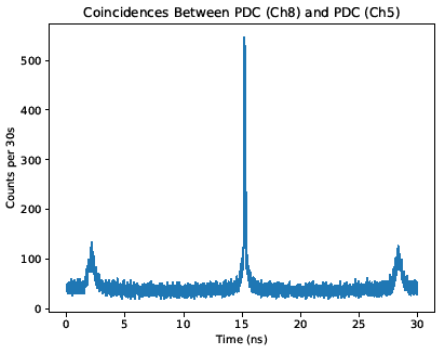

Fig. 22. Exemplary coincidence measurements between the signal and idler channel result in peaks separated by the pump laser repetition rate (13 ns).

These aMZIs feature a variable optical attenuator in the short arm to balance the power in both arms. A voltage lower than 1V is required to achieve visibilities of around 97% which is more than enough for time-bin entanglement. Additionally, the aMZIs are equipped with phase shifters needed for time-bin state tomography. The aMZIs still suffer from high transmission losses on the order of -10 dB and phase instability due to the heating of the chip when the attenuator or phase shifter are active. Time-bin entanglement characterization measurements are ongoing and will be reported soon.

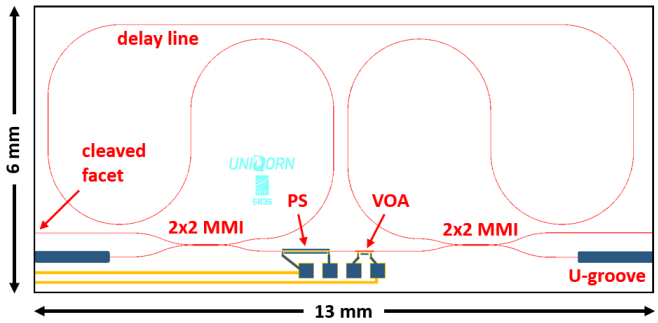

Fig. 23 Layout of the asymmetric Mach-Zehnder interferometer. The phase shifter (PS) and the variable optical attenuator (VOA) are the controls of the interferometer, which is formed by connecting to multi-mode interference (MMI) devices.

VI. CONCLUSION

Different photonic integration platforms have been thoroughly investigated within the Quantum Technology Flagship project UNIQORN for quantum communication applications. These are: indium phosphide platform, CMOS-compatible silicon platform and the more recently developed polymer-based hybrid integration platform.

The hybrid polyboard platform was used to manufacture a QRNG module. About 70% randomness extraction has been achieved with off-chip SPADs in a 1x4 QRNG on chip. Furthermore, a 1x16 QRNG module has been produced and coupled to an array of 32 SPADs, featuring onboard coincidence logic. A preliminary characterization successfully demonstrates the hybrid integration method.

Moreover, a QKD transmitter based on InP platform has been designed, manufactured and tested in a QKD setup achieving a secure rate of 1 kbit/s, indicating that InP is a valid choice for QKD transmitters used for phase and time-bin encoding.

A transimpedance amplifier based on gallium arsenide was designed and fabricated. Preliminary characterizations showed an exceptional large electrical noise clearance of 28 dB at 100 MHz. The transimpedance amplifier is the key component for a CV QKD receiver, strongly determining the noise and speed figures of merit.

In addition to the QRNG application, the polyboard platform has been investigated as a host platform for integrated non-classical photon sources. Promising results have been obtained in heralded photon source, polarization, and time-bin entangled photon sources.

To conclude, during the Quantum Flagship ramp-up phase, the UNIQORN project has been further pushing the state-of-the-art of quantum PICs in the considered integration platforms for quantum communication applications. We envision that in the next phase of the Quantum Flagship new generations of devices will be manufactured based on the findings presented here, further solidifying the integrated quantum photonic approach for quantum technologies.

REFERENCES

[1] M. A. Nielsen and I. Chuang "Quantum computation and quantum information," Cambridge University Press, 2011.

[2] N. Gisin and R. Thew "Quantum communication," *Nat. Photonics*, vol. 1, pp 165-171, 2007.

[3] E. Pelucchi *et al.*, "The potential and global outlook of integrated photonics for quantum technologies," *Nat. Rev. Phys.*, vol. 4, pp 194-208, 2022

[4] https://quantum-uniqorn.eu/.

[5] D. de Felipe *et al.*, "Recent developments in polymer-based photonic components for disruptive capacity upgrade in data centers," *J. Light. Technol.*, vol. 35, no.4, 2017.

[6] M. Ghioni *et al.*, "Progress in silicon single-photon avalanche diodes," *IEEE J. Sel. Top. Quantum Electron.*, vol. 13, no. 4, 2007.

[7] D. Frauchiger, R. Renner and M. Troyer, "True randomness from realistic quantum devices," *arXiv preprint*, arXiv:1311.4547, 2013.

[8] X. Zhang, Y.Q. Nie, H. Liang and J. Zhang, "FPGA implementation of Toeplitz hashing extractor for real time post-processing of raw random numbers." In *2016 IEEE-NPSS Real Time Conference (RT)*, pp. 1-5. IEEE, 2016.

[9] L. Bassham *et al.*, "A Statistical Test Suite for Random and Pseudorandom Number Generators for Cryptographic Applications" Special Publication (NIST SP), National Institute of Standards and Technology, Gaithersburg, MD, 2010

[10] H. O. Çirkinoglu, R. Santos, K. Williams, and X. Leijtens, "Monolithically integrated differential phase shift transmitter for quantum key distribution," *In Proc. ECIO, 22nd European Conference on Integrated Optics*, 2020.

[11] H.O Çirkinoglu, R. Santos, K. Williams, and X. Leijtens, "An InP-based integrated modulated coherent state source for differential phase shift quantum key distribution," *in 24th Annual Symposium of the IEEE Photonics Benelux Chapter*, 2019.

[12] D. Zhao, "High-precision Distributed Bragg Reflectors in a Generic Photonics Integration Platform". PhD thesis, Eindhoven University of Technology, Eindhoven, The Netherlands, 2018. ISBN 978-90-386-4627-5.

[13] M. Smit *et al.*, "An introduction to InP-based generic integration technology," *Semicond. Sci. Technol.*, vol. 29, 2014.

[14] "Smart Photonics", http://smartphotonics.nl.

[15] S. Latkowski *et al.*, "Open standards for automation of testing of photonic integrated circuits," *IEEE J. Sel. Top. Quantum Electron.*, vol. 25, no. 5, 2019.

[16] P. Eraerds *et al.*, "Quantum key distribution and 1 Gbps data encryption over a single fibre," *New J. Phys.*, vol. 12, no. 6, 2010.

[17] C. H. Bennett and G. Brassard, "Quantum cryptography: Public key distribution and coin tossing". In *Proceedings of IEEE International Conference on Computers, Systems and Signal Processing*, volume 175, page 8. New York, 1984.

[18] M. Peev *et al.*, "The SECOQC quantum key distribution network in Vienna," *New J. Phys.*, vol 11, 2009.

[19] M. Sasaki *et al.*, "Field test of quantum key distribution in the tokyo qkd network," *Opt. Express*, vol. 19, no. 11, pp. 10 387–10 409, 2011.

[20] D. Stucki *et al*., "Fast and simple one-way quantum key distribution," *Appl. Phys. Lett.*, vol. 87, 194108, 2005.

[21] K. Inoue, E. Waks and Y. Yamamoto, "Differential phase shift quantum key distribution." *Phys. Rev. Lett.*, vol. 89, 2002.

[22] R. H. Hadfield, "Single-photon detectors for optical quantum information applications." *Nat. Photonics*, vol. 3, 696-705, 2009.

[23] F. Laudenbach *et al.*, "Continuous-variable quantum key distribution with Gaussian modulation—The theory of practical implementations," *Adv. Quantum Technol.*, vol. 1, 2018.

[24] Y. Wang, X. Chen, and L. Zhang, "High-speed balanced homodyne detector for quantum information applications," *J. Phys. Conf. Ser.*, vol. 844, 12010, 2017.

[25] J. F. Tasker *et al*., "Silicon photonics interfaced with integrated electronics for 9 GHz measurement of squeezed light," *Nat. Photonics*, vol. 15, 11–15, 2021.

[26] C. Bruynsteen, M. Vanhoecke, J. Bauwelinck, and X. Yin, "Integrated balanced homodyne photonic–electronic detector for beyond 20 GHz shot-noise-limited measurements," *Optica*, vol. 8, no. 9, pp. 1146–1152, 2021.

[27] A. Antonopoulos *et al.*, "CMOS small-signal and thermal noise modeling at high frequencies," *IEEE Trans. Electron Devices*, vol. 60, issue 11, 3726–3733, 2013.

[28] S. Voinigescu, "High-Frequency Integrated Circuits", Cambridge University, 2013.

[29] F. Raffaelli, G. Ferranti, D. H. Mahler, P. Sibson, J. E. Kennard, A. Santamato, G. Sinclair, D. Bonneau, M. G. Thompson, and J. C. Matthews, "A homodyne detector integrated onto a photonic chip for measuring quantum states and generating random numbers," Quantum Sci. Technol. 3, 025003 (2018).

[30] D. Huang, J. Fang, C. Wang, P. Huang, and G. H. Zeng, "A 300-MHz bandwidth balanced homodyne detector for continuous variable quantum key distribution," Chin. Phys. Lett. 30, 114209 (2013).

[31] S. Andreou, K. A. Williams and E. A. J. M. Bente, "Electro-optic tuning of a monolithically integrated widely tuneable InP laser with free-running and stabilized operation," *J. Light. Technol.*, vol. 38, issue 7, 2019.

[32] H. O. Çirkinoglu, R. Santos, K. Williams, and X. Leijtens. "Monolithically integrated InP optical 90° hybrid", *in 25th Annual Symposium of the IEEE Photonics Benelux Chapter 2021*, to be published.

[33] S. Krapick, H. Herrmann, V. Quiring, B. Brecht, H. Suche and C. Silberhorn, "An efficient integrated two-color source for heralded single photons," *New. J. Phys.*, vol. 15, 2013.

[34] F. Laudenbach, S. Kalista, M. Hentschel, P. Walther and H. Hübel, "A novel single-crystal & single-pass source for polarisation-and colour-entangled photon pairs," *Sci. Rep.*, vol. 7, no. 7235, 2017.

[35] H. Chen *et al*., "Invited Article: Time-bin entangled photon pairs from Bragg-reflection waveguides," *APL Photonics*, vol. 3, issue 8, 2018.